

## Origin of hydrodynamic instability from noise: From laboratory flow to accretion disk

Subham Ghosh\* and Banibrata Mukhopadhyay<sup>†</sup>

*Department of Physics, Indian Institute of Science, Bangalore 560012, India*



(Received 28 January 2020; accepted 23 December 2020;  
published 19 January 2021)

We attempt to address the old problem of plane shear flows: the origin of turbulence and hence transport of angular momentum in accretion flows as well as laboratory flows, such as plane Couette flow. We undertake the problem by introducing an extra force in Orr-Sommerfeld and Squire equations along with the Coriolis force mimicking the local region of the accretion disk. For plane Couette flow, the Coriolis term drops. Subsequently we solve the equations with the WKB approximation method. We investigate the dispersion relation for the Keplerian flow and plane Couette flow for all possible combinations of wave vectors. Due to the very presence of extra force, we show that both flows are unstable for a certain range of wave vectors. However, the nature of instability between the flows is different. We also study the Argand diagrams of the perturbation eigenmodes. This helps us to compare the different timescales corresponding to the perturbations as well as accretion. We ultimately conclude with this formalism that fluid gets enough time to be unstable and hence plausibly turbulent particularly in the local regime of the Keplerian accretion disks. Repetition of the analysis throughout the disk explains the transport of angular momentum and matter along outward and inward directions, respectively.

DOI: [10.1103/PhysRevFluids.6.013903](https://doi.org/10.1103/PhysRevFluids.6.013903)

### I. INTRODUCTION

A long-standing mismatch between theory and experiment regarding the transition from laminar to turbulent flows for laboratory fluids, e.g., plane Couette flow and plane Poiseuille flow, exists in the literature. The linear theory of perturbation says that plane Poiseuille flow becomes unstable beyond Reynolds number (Re) 5772.22 [1] and, on the other hand, plane Couette flow is stable for any Re [2]. However, according to experiments/simulations, beyond  $Re \sim 1000$  [3,4] and  $Re \sim 350$  [5,6] the laminar flow becomes turbulent in the case of plane Poiseuille flow and plane Couette flow, respectively. A similar kind of mismatch exists in the context of astrophysics, particularly in case of accretion disks. Accretion disks are astrophysical objects formed around a denser object mainly in the form of a disk. Nevertheless, the accretion disk involves very sophisticated (or rich) physics behind the formation and evolution of its various parts depending on the nature of the central objects (black holes, white dwarfs, neutron stars, main sequence stars, etc.) around which the matter accretes in the form of a disk. The physics also involves the nature of mass supply (e.g., mass supplied from evolved stars, the interstellar medium, molecular clouds, etc.) that aids accretion around the central object. However, in this work, we shall be discussing a geometrically thin and optically thick disk, where the accreting matter almost follows Kepler's law, i.e., the fluid particle in the corresponding flow revolves around the central object at a particular radius due to the almost balance between

---

\*subham@iisc.ac.in

†bm@iisc.ac.in

inward gravitational force and outward centrifugal force. The flow therefore is called Keplerian flow. The change in the angular momentum per unit mass of the fluid particle, therefore, occurs in increasing proportion to the square root of the radial distance of the particle. Due to the very nature of the Keplerian rotation, the perturbation of the fluid particle decays and eventually the particle returns to its initial position. This is called Rayleigh stability. The Keplerian flow, therefore, is Rayleigh stable.

However, due to the Keplerian rotation, two fluid layers across the radial direction in the disk will have different angular velocities. Since the flow has differential velocity across the radial direction, molecular viscosity comes into the picture. However, observational evidence, e.g., temperature, luminosity, etc., from the Keplerian accretion disk do not support the molecular viscosity as the origin of matter transport. The molecular viscosity is so weak that it cannot transport the angular momentum outward and matter inward and hence cannot explain the observables [7]. The belief is that it is the turbulent viscosity which is behind the transport. This idea was put forward by Shakura and Sunyaev [8] and Lynden-Bell and Pringle [9] without explicitly revealing the reason behind the turbulence. In 1991 Balbus and Hawley [10] came up with an idea of an instability mechanism due to the interplay between weak magnetic field and the rotation of the fluid parcel, naming magneto-rotational instability (MRI), following the idea of Velikhov [11] and Chandrasekhar [12]. In spite of the overwhelming success of MRI in explaining the origin of turbulence, it is not lacking caveats. In the colder systems, e.g., a protoplanetary disk [13,14], cataclysmic variables in their low states [15,16], the outer part of active galactic nucleus (AGN) disks, and the underlying dead zone [17], where the ionization is very small such that matter cannot be coupled with the magnetic field, MRI gets suppressed. It is not only the low ionization that challenges MRI; there are, in fact, many other examples too. Nath and Mukhopadhyay [18] argued that it is the magnetic transient growth that brings nonlinearity and hence plausible turbulence in the system beyond  $Re = 10^9$ , since their growth rate is faster than MRI in that regime. Usually,  $Re$  in accretion disks [19] is larger than this value, hence the relevance of MRI in large  $Re$  systems is questionable. As a general point of interest, the transient energy growth in the case of magnetohydrodynamical shear flows (with viscosity and resistivity included) was studied further by Bhatia and Mukhopadhyay [20]. They showed that even transient energy growth ceased to occur beyond a certain magnetic field. In addition to this, Pessah and Psaltis [21] and Das *et al.* [22], using local and global analysis, respectively, showed the stabilization of the axisymmetric MRI above a certain magnitude of a toroidal component of the magnetic field for compressible and differentially rotating flows. It is, therefore, of great concern whether there is any instability in the system from a hydrodynamical origin.

However, in the literature [23–34], there is a long-standing debate regarding the stability of Rayleigh stable flows, particularly in the context of accretion disks. Approximating the local hot accretion flow to be shearing sheet, researchers [35,36] attempted, analytically and with simulation, to resolve the issue without considering viscosity. They concluded that the sustained turbulence and hence outward transport of angular momentum were not possible in the Keplerian flow if hydrodynamics was considered only. However, Lesur and Longaretti [37], with shearing sheet approximation and considering viscosity strongly, disagreed with the aforementioned authors and claimed that the absence of turbulence in the simulation in the above-mentioned works was resolution issue. Although they agreed that there was a lack of computer resources to resolve the Keplerian regime, their extrapolated numerical data could not produce astrophysically sufficient subcritical turbulent transport in the Keplerian flow. Pumir [38], however, claimed for sustained turbulence if the mean flow follows the plane Couette flow profile. However, they did not consider rotational effects. Fromang and Papaloizou [39], though they did magnetohydrodynamical (MHD) simulation, argued for considering explicit diffusion coefficients, both resistive and viscous, whose effect is stronger than the numerical dissipation effect, before making any conclusion based on MHD simulation. Therefore, we notice that in all of these works some important physics are missing: viscosity [35,36], resolution of the Keplerian region [37], the Coriolis force [38], explicit diffusion coefficients (both viscous and resistive) [39] are not adequately considered. Even if we

have well-resolved simulations [40–42], the previously mentioned facts or parameter regions, where MRI is inapplicable or insufficient as an instability mechanism, do exist. Nevertheless, the authors argued for plausible emergence of hydrodynamics instability and hence further turbulence through experiment (e.g., Ref. [43]), simulations in the context of accretion disks (e.g., Ref. [44]), and transient growth in the case of otherwise linearly stable flows (e.g., Refs. [33,45–47]).

We, therefore, search for a hydrodynamical origin of nonlinearity and hence plausible turbulence in the accretion disk. We, in particular, consider an extra force in this work, and the force has a stochastic origin. The existence and consequences of the stochastic force in the hydrodynamical systems were initiated by Mukhopadhyay and Chattopadhyay [34] inspired by the idea of Nelson and Foster [48] and DeDominicis and Martin [49]. They showed that the presence of the stochastic force in the rotating shear flows in a narrow gap limit reveals large correlation of energy growth of the perturbation. Later, Nath and Mukhopadhyay [50] obtained the dispersion relation of the linear perturbations considering stochastic force in the Orr-Sommerfeld and Squire equations, describing the fluid flow in a small radial patch of the accretion disk. However, they considered the plane wave perturbation with a constant amplitude as the trial solution of the Orr-Sommerfeld and Squire equations. In the present work, we consider three-dimensional perturbations and the WKB approximation to obtain the solutions for Orr-Sommerfeld and Squire equations. While qualitatively we obtain similar result as Nath and Mukhopadhyay [50], it brings quantitative insight which is useful to infer observed data and/or experimental results based on our model. We also obtain the Argand diagrams corresponding to the perturbations, and these are necessary to compare the timescales corresponding to the growth with those of oscillation of the perturbations. In addition to this, we also confirm whether the fluid parcel inside the shearing box within a small patch of accretion disk gets enough time to enter into the nonlinear regime and hence becomes turbulent within the timescale it came across the box. However, for plane Couette flow, we do not need to worry about any such timescale, as there is no radial infall.

The plan of the paper is the following. In Sec. II we describe the governing equations, which are Orr-Sommerfeld and Squire equations in the presence of Coriolis force and noise for linearly perturbed flow inside a shearing box at a smaller patch of accretion disk. We then write them in the Fourier space to obtain a general dispersion relation. In Sec. III the dispersion relation is studied extensively for the Keplerian and plane Couette flows. The Argand diagrams corresponding to the linear perturbations in the case of Keplerian flow are studied in Sec. IV for various parameters. In the end, we discuss the plausibility of occurrence of instability, which could lead further to nonlinearity and hence turbulence in the context of accretion disks and laboratory flows, e.g., plane Couette flows in Sec. V. We finally conclude in Sec. VI that our model is able to explain the origin of instability and hence turbulence in the context of accretion disk as well as plane Couette flow.

## II. FORMALISM

The detailed description of the local formulation can be found in Mukhopadhyay *et al.* [45] and in Bhatia and Mukhopadhyay [20]. The schematic diagram of the background flow inside the shearing box is shown in Ref. [33]. As the fluid is in the local region, we assume the fluid to be incompressible [18,46]. There we recast the Navier-Stokes equation in Orr-Sommerfeld and Squire equations in the presence of Coriolis force and extra force by eliminating the pressure term from different components of the Navier-Stokes equation and utilizing the continuity equation for incompressible flow [50]. The ensemble-averaged Orr-Sommerfeld and Squire equations in the presence of Coriolis force and extra force are given by

$$\left(\frac{\partial}{\partial t} + U \frac{\partial}{\partial y}\right) \nabla^2 u - \frac{\partial^2 U}{\partial x^2} \frac{\partial u}{\partial y} + \frac{2}{q} \frac{\partial \zeta}{\partial z} = \frac{1}{\text{Re}} \nabla^4 u + \eta_1, \quad (1)$$

$$\left(\frac{\partial}{\partial t} + U \frac{\partial}{\partial y}\right) \zeta - \left(\frac{\partial U}{\partial x} + \frac{2}{q}\right) \frac{\partial u}{\partial z} = \frac{1}{\text{Re}} \nabla^2 \zeta + \eta_2, \quad (2)$$

where  $U = -x$  is the  $y$  component of background velocity. The other components of background velocity are zero;  $u$  and  $\zeta$  are  $x$  components of velocity and vorticity perturbations, respectively;  $q$  is the rotation parameter which describes the radial dependence of the angular frequency of fluid element around the central object, given by  $\Omega \propto 1/r^q$ ;  $\text{Re}$  is the Reynolds number;  $\eta_1$  and  $\eta_2$  are the extra forces on the fluid particles.  $q$  becomes 1.5 and  $\infty$  for the Keplerian and plane Couette flows [20,45] respectively. In order to obtain the dispersion relation, we write the above equations in the Fourier space. Our conventions for Fourier transform and inverse Fourier transform are, respectively,

$$A(\mathbf{r}, t) = \int \tilde{A}_{\mathbf{k}, \omega} e^{i(\mathbf{k}\cdot\mathbf{r} - \omega t)} d^3k d\omega \quad (3)$$

and

$$\tilde{A}_{\mathbf{k}, \omega} = \left(\frac{1}{2\pi}\right)^4 \int A(\mathbf{r}, t) e^{-i(\mathbf{k}\cdot\mathbf{r} - \omega t)} d^3x dt. \quad (4)$$

Here  $A$  can be any one of  $u$ ,  $\zeta$ , and  $\eta_i$ ;  $\mathbf{k}$  and  $\omega$  are the wave vector and frequency, respectively, in Fourier space such that in Cartesian coordinates  $\mathbf{k} = (k_x, k_y, k_z)$  and  $|\mathbf{k}| = k$ ;  $\mathbf{r}$  is the position vector and in Cartesian coordinates  $\mathbf{r} = (x, y, z)$ .

The boundary conditions to solve Eqs. (1) and (2) are

$$u = \frac{\partial u}{\partial x} = \zeta = 0, \quad \text{at } x = \pm 1. \quad (5)$$

In Fourier space, Eqs. (1) and (2) become

$$k_y k^2 \frac{\partial \tilde{u}_{\mathbf{k}, \omega}}{\partial k_x} = \left(i\omega k^2 - 2k_x k_y - \frac{k^4}{\text{Re}}\right) \tilde{u}_{\mathbf{k}, \omega} + \frac{2ik_z}{q} \tilde{\zeta}_{\mathbf{k}, \omega} - m_1 \delta(\mathbf{k}) \delta(\omega), \quad (6)$$

$$k_y \frac{\partial \tilde{\zeta}_{\mathbf{k}, \omega}}{\partial k_x} = -ik_z \left(1 - \frac{2}{q}\right) \tilde{u}_{\mathbf{k}, \omega} + \left(i\omega - \frac{k^2}{\text{Re}}\right) \tilde{\zeta}_{\mathbf{k}, \omega} + m_2 \delta(\mathbf{k}) \delta(\omega), \quad (7)$$

where the Fourier transform of  $\eta_i$  is  $m_i \delta(\mathbf{k}) \delta(\omega)$  with  $m_i$  being the constant mean corresponding to  $\eta_i$ . The traveling wave solutions for Eqs. (1) and (2) are assumed to be

$$u = u(x) e^{i(\boldsymbol{\alpha}\cdot\mathbf{r} - \beta t)}, \quad \zeta = \zeta(x) e^{i(\boldsymbol{\alpha}\cdot\mathbf{r} - \beta t)}, \quad (8)$$

where the wave vector,  $\boldsymbol{\alpha}$ , is given by  $\boldsymbol{\alpha} = (\alpha_1, \alpha_2, \alpha_3)$ , and  $\beta$  is the frequency. Usually  $\beta$  is a complex quantity and, according to our convention, if the imaginary part of  $\beta$ , i.e.,  $\text{Im}(\beta)$ , is positive, then the perturbation grows with time. To obtain the dispersion relation, we transform Eq. (8) in the Fourier space (see the Appendix) and substitute them in Eqs. (6) and (7), and then we integrate with respect to  $\omega$  and  $k$ . See the Appendix for details. We further use the WKB approximation to obtain the solution. Therefore, we neglect second- and higher-order derivatives, as they are varying slowly over the length  $1/\alpha_1$ . The dispersion relations from Eqs. (6) and (7) are then

$$\begin{aligned} \left(i\beta\alpha^2 - \frac{\alpha^4}{\text{Re}}\right) u(0) + 2i\alpha_1 \left(\frac{2\alpha^2}{\text{Re}} - i\beta\right) u'(0) + \frac{2i\alpha_3}{q} \zeta(0) - m_1 &= 0, \\ -i\alpha_3 \left(1 - \frac{2}{q}\right) u(0) + \left(i\beta - \frac{\alpha^2}{\text{Re}}\right) \zeta(0) + \frac{2i\alpha_1}{\text{Re}} \zeta'(0) + m_2 &= 0. \end{aligned} \quad (9)$$

Here  $u(0)$  and  $u'(0)$  are, respectively, values of  $u(x)$  and  $u'(x)$  at  $x = 0$ . We also consider the first-order derivatives to be

$$u'(0) = \gamma u(0) = \gamma u_0, \quad \zeta'(0) = \gamma \zeta(0) = \gamma \zeta_0,$$

and the same strength for the extra forces, i.e.,  $m_1 = m_2 = m$ . Now if we eliminate  $\zeta$  with all the assumptions from Eqs. (6) and (7), we obtain the dispersion relation, which is given by

$$m \left( 2\alpha_3 + \beta q + \frac{i\alpha^2 q}{\text{Re}} + \frac{2\alpha_1 \gamma q}{\text{Re}} \right) = u_0 \left( 2i\alpha_3^2 + i\alpha^2 \beta^2 q + 2\alpha_1 \beta^2 \gamma q - \frac{4i\alpha_3^2}{q} - \frac{i\alpha^6 q}{\text{Re}^2} - \frac{6\alpha_1 \alpha^4 \gamma q}{\text{Re}^2} + \frac{8i\alpha_1^2 \alpha^2 \gamma^2 q}{\text{Re}^2} - \frac{2\alpha^4 \beta q}{\text{Re}} + \frac{8i\alpha_1 \alpha^2 \beta \gamma q}{\text{Re}} + \frac{4\alpha_1^2 \beta \gamma^2 q}{\text{Re}} \right). \quad (10)$$

For clarity, we consider  $\gamma = \pm 1, \pm \alpha_1, \pm i\alpha_1$ . However, only  $\gamma = i\alpha_1$  gives  $\text{Im}(\beta) < 0$  for any  $\text{Re}$  without extra force is considered, i.e.,  $m = 0$ , which is physical. We, therefore, stick to  $\gamma = i\alpha_1$  throughout the paper. For computational purposes, we consider the components of wave vectors along the  $y$  direction to be zero, i.e.,  $\alpha^2 = \alpha_1^2 + \alpha_3^2$ . However, if we make  $\alpha_3 = 0$  and  $\alpha^2 = \alpha_1^2 + \alpha_2^2$ , from Eq. (9) it is clear that the problem will become qualitatively plane Couette flow.

### III. DISPERSION RELATION

#### A. Keplerian flow

Here we shall study the solutions of Eq. (10) for different parameters. Equation (10) is a quadratic equation of  $\beta$  with complex coefficients. Among the two solutions of  $\beta$ , the one which we are interested in is

$$\beta = -\frac{0.5i}{3\alpha_1^2 q + \alpha_3^2 q} \left[ \frac{mq}{u_0} + \frac{14\alpha_1^4 q}{\text{Re}} + \frac{12\alpha_3^2 \alpha_1^2 q}{\text{Re}} + \frac{2\alpha_3^4 q}{\text{Re}} - \frac{1}{\text{Re}} \left( \frac{24i\alpha_3 \alpha_1^2 m q \text{Re}^2}{u_0} + \frac{8i\alpha_3^3 m q \text{Re}^2}{u_0} + \frac{m^2 q^2 \text{Re}^2}{u_0^2} - \frac{8\alpha_1^4 m q^2 \text{Re}}{u_0} + 16\alpha_1^8 q^2 + 24\alpha_3^2 \alpha_1^2 q \text{Re}^2 + 8\alpha_3^4 q \text{Re}^2 - 48\alpha_3^2 \alpha_1^2 \text{Re}^2 - 16\alpha_3^4 \text{Re}^2 \right)^{\frac{1}{2}} \right]. \quad (11)$$

The other solution of  $\beta$  is always stable irrespective of extra force. However, Eq. (11) expectedly provides negative  $\text{Im}(\beta)$  for  $m = 0$  irrespective of  $\text{Re}$ . Interestingly, Eq. (11) also provides positive  $\text{Im}(\beta)$  within a particular window of  $\alpha_1$  and  $\alpha_3$  beyond certain  $m$  depending on  $\text{Re}$  for a fixed  $q$ . Here we observe the dispersion relations, i.e., the variation of  $\text{Im}(\beta)$  as a function of  $\alpha_1$  and  $\alpha_3$  for different  $\text{Re}$  and  $m/u_0$  for the Keplerian flow. Figures 1 and 2 show the variation of  $\text{Im}(\beta)$  as a function of  $\alpha_1$  and  $\alpha_3$  for the Keplerian and plane Couette flow (see Sec. III B), respectively, for  $m/u_0 = 0$ . From linear stability analysis, we know these two flows are stable for any  $\text{Re}$ , and this is confirmed in Figs. 1 and 2. The kinks in Fig. 1 around  $\alpha_3 = 0$  are there for  $q < 2$ , and hence their presence is due to the rotation in the system.

The color codes that we use for the contour plots for Figs. 1 to 6 are the following. We use blues and reds to indicate  $\text{Im}(\beta)$ 's negativity and positivity, respectively. We use white to indicate the transition from the negative to positive of  $\text{Im}(\beta)$ .

As we introduce the extra force, i.e.,  $m \neq 0$ ,  $\text{Im}(\beta)$  becomes positive for a particular range of  $\alpha_1$  and  $\alpha_3$ . Throughout the paper, we use  $\text{Im}(\beta)_{\text{max}}$  and  $\text{Re}(\beta)_{\text{max}}$  to indicate the maximum value of  $\text{Im}(\beta)$  and at which  $\text{Re}(\beta)$  it occurs, respectively. Figures 3 and 4 show the variation of  $\text{Im}(\beta)$  as a function of  $\alpha_1$  and  $\alpha_3$  for  $m/u_0 = 10$  for the Keplerian flow but for  $\text{Re} = 10^2$  and  $10^{10}$ , respectively. Figures 5 and 6 show the variation of  $\text{Im}(\beta)$  as a function of  $\alpha_1$  and  $\alpha_3$  for  $\text{Re} = 10^4$  for the Keplerian flow but for  $m/u_0 = 10$  and  $10^2$ , respectively. These two figures depict that the increment of  $m/u_0$  increases the  $\text{Im}(\beta)$  value for a fixed  $\text{Re}$ . Note that the bounds on the axes of Figs. 4 and 5 are different than that of Figs. 3 and 6. The reason is described later in this section.

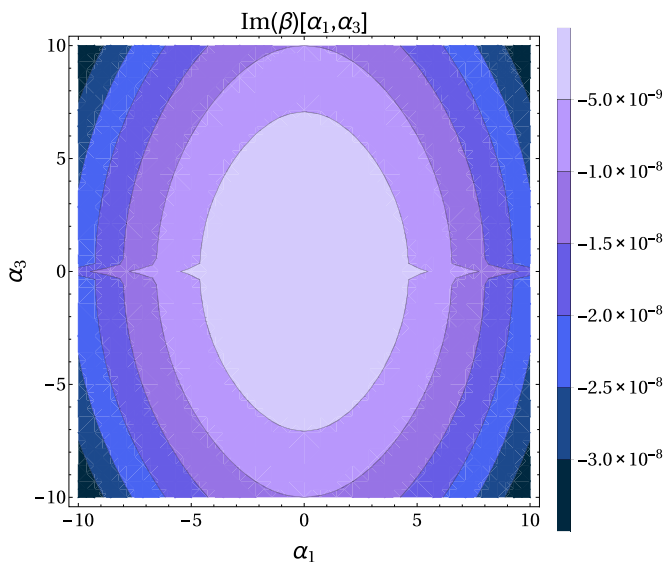


FIG. 1. Variation of  $\text{Im}(\beta)$  as a function of  $\alpha_1$  and  $\alpha_3$  for  $\text{Re} = 10^{10}$  and  $m/u_0 = 0$  for the Keplerian flow.

Now if we fix  $m/u_0$  and increase  $\text{Re}$ , it is expected that the value of  $\text{Im}(\beta)$  increases. Figures 7, 8, 9, and 10 depict the same. These four figures show the variation of  $\text{Im}(\beta)$  as a function of  $\alpha_1$  and  $\alpha_3$  in three dimensions for  $\text{Re} = 10, 10^2, 10^3$  and  $10^4$  for  $m/u_0 = 10$  in the case of the Keplerian flow.  $\text{Im}(\beta)_{\max}$  is given in the caption corresponding to each figure to compare one with other. We make three-dimensional plots for these cases to capture  $\text{Im}(\beta)_{\max}$ , as it is not obvious from the contour plots, particularly from Figs. 3 and 4. This fact becomes clear once we compare Figs. 5 and 10. From these four three-dimensional figures and from Figs. 3, 5, and 4, it is clear that the increment of  $\text{Re}$  for a fixed  $m/u_0$  also increases the range of  $\alpha_1$  and  $\alpha_3$  which could give rise to

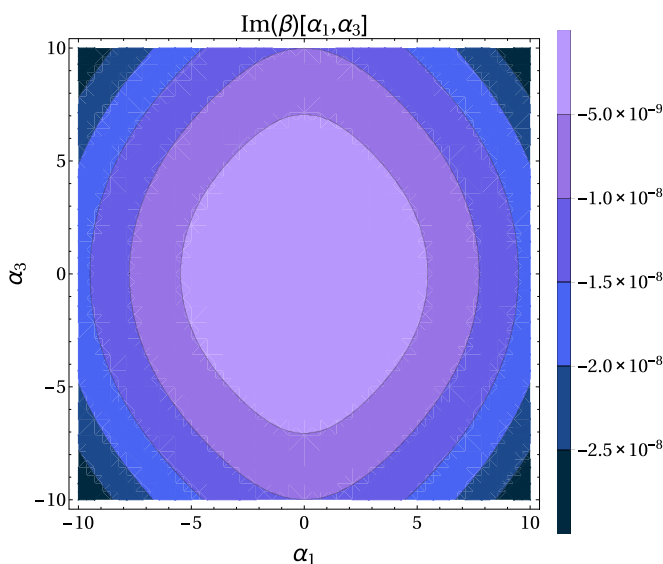


FIG. 2. Variation of  $\text{Im}(\beta)$  as a function of  $\alpha_1$  and  $\alpha_3$  for  $\text{Re} = 10^{10}$  and  $m/u_0 = 0$  for plane Couette flow.

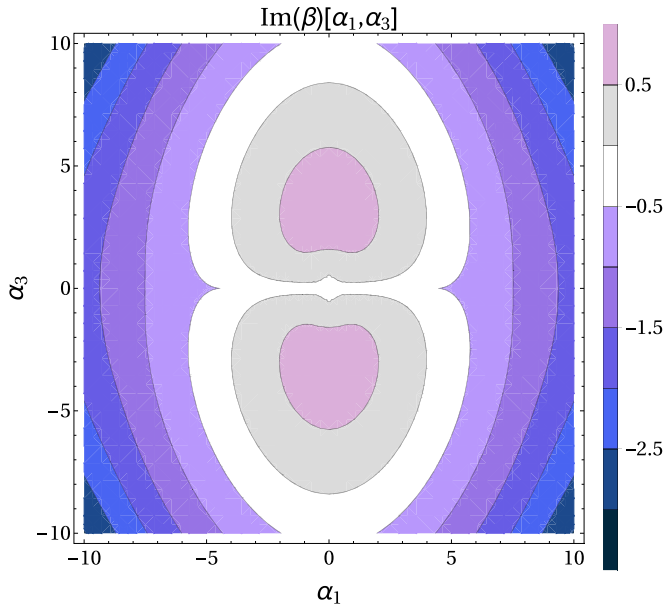


FIG. 3. Variation of  $\text{Im}(\beta)$  as a function of  $\alpha_1$  and  $\alpha_3$  for  $\text{Re} = 10^2$  and  $m/u_0 = 10$  for the Keplerian flow.

positive  $\text{Im}(\beta)$  and hence instability in the system. To capture this particular fact, we zoom out the axes of Figs. 4 and 5 as these two figures look almost similar if the bound on the axes is chosen from  $-10$  to  $10$ . Similarly, Figs. 9 and 10 may apparently look same, but they are not. If we check the fact at which value of  $\text{Im}(\beta)$  the surfaces of  $\text{Im}(\beta)$  corresponding to these two figures cut the

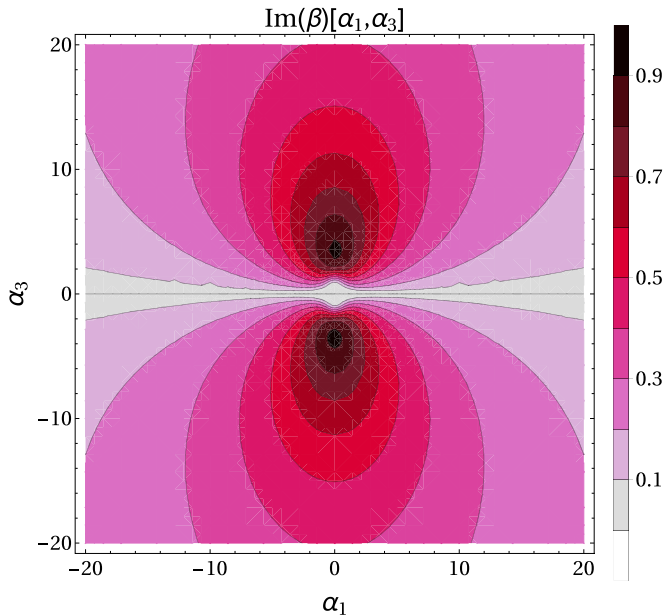


FIG. 4. Variation of  $\text{Im}(\beta)$  as a function of  $\alpha_1$  and  $\alpha_3$  for  $\text{Re} = 10^{10}$  and  $m/u_0 = 10$  for the Keplerian flow.

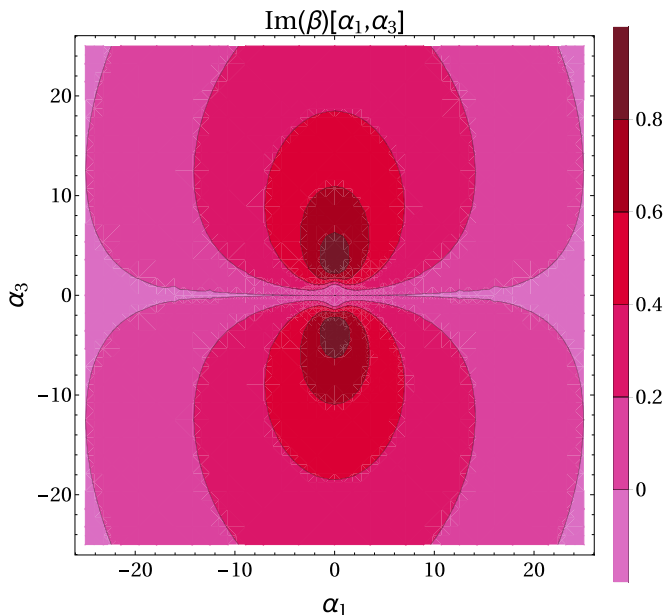


FIG. 5. Variation of  $\text{Im}(\beta)$  as a function of  $\alpha_1$  and  $\alpha_3$  for  $\text{Re} = 10^4$  and  $m/u_0 = 10$  for the Keplerian flow.

$\text{Im}(\beta)$  axis at  $\alpha_1 = -10$ , then we can be sure that they are not same. Apart from this, Fig. 9 shows that at  $\alpha_1 = -10$ , the surface of  $\text{Im}(\beta)$  is downwards while the same for Fig. 10 is almost flat.

However,  $\text{Im}(\beta)_{\max}$  does not increase beyond 0.91, even if we increase  $\text{Re}$  for  $m/u_0 = 10$  for the Keplerian flow. It, therefore, looks like  $\text{Im}(\beta)_{\max}$  gets saturated at 0.91 at  $\text{Re} = 10^4$ , and any further increment in  $\text{Re}$  increases only the range of  $\alpha_1$  and  $\alpha_3$  that makes  $\text{Im}(\beta)$  positive. This

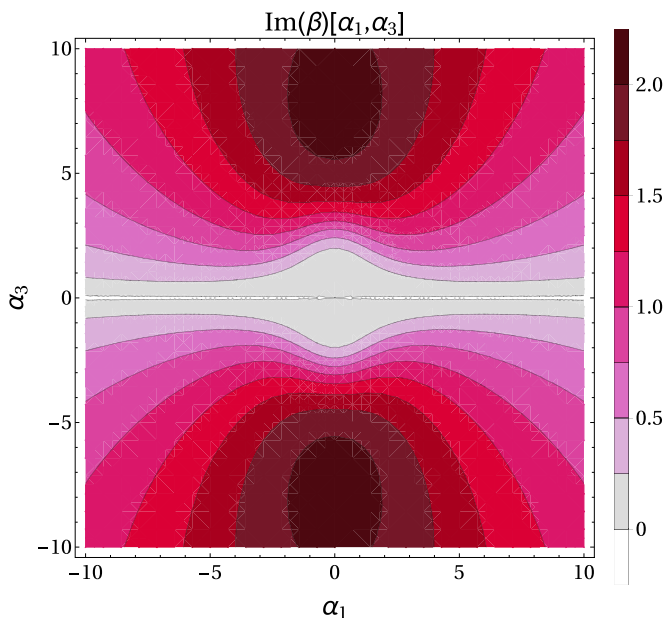


FIG. 6. Variation of  $\text{Im}(\beta)$  as a function of  $\alpha_1$  and  $\alpha_3$  for  $\text{Re} = 10^4$  and  $m/u_0 = 10^2$  for the Keplerian flow.

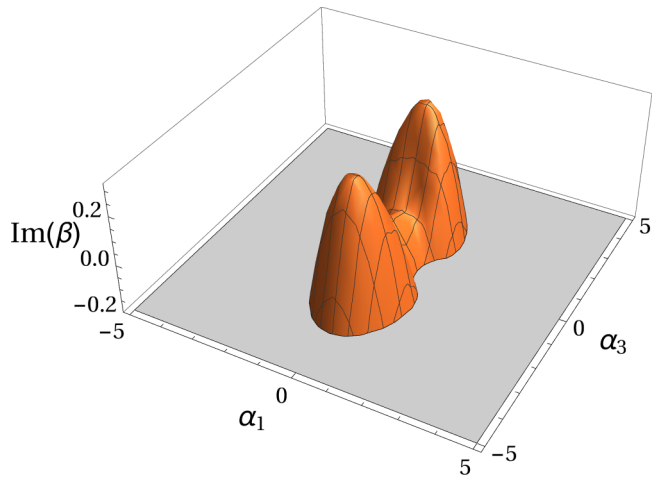


FIG. 7. Variation of  $\text{Im}(\beta)$  in three dimensions as a function of  $\alpha_1$  and  $\alpha_3$  for  $\text{Re} = 10$  and  $m/u_0 = 10$  for the Keplerian flow.  $\text{Im}(\beta)_{\text{max}} = 0.33$ .

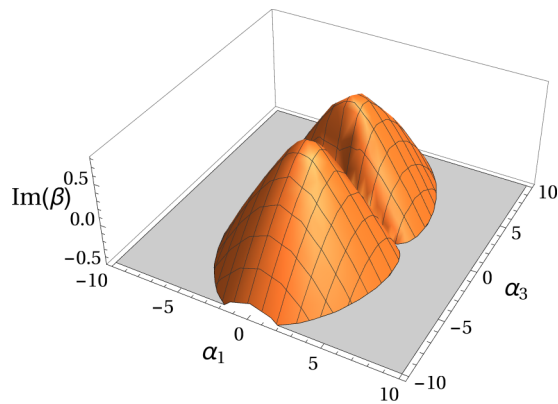


FIG. 8. Variation of  $\text{Im}(\beta)$  in three dimensions as a function of  $\alpha_1$  and  $\alpha_3$  for  $\text{Re} = 10^2$  and  $m/u_0 = 10$  for the Keplerian flow.  $\text{Im}(\beta)_{\text{max}} = 0.822$ .

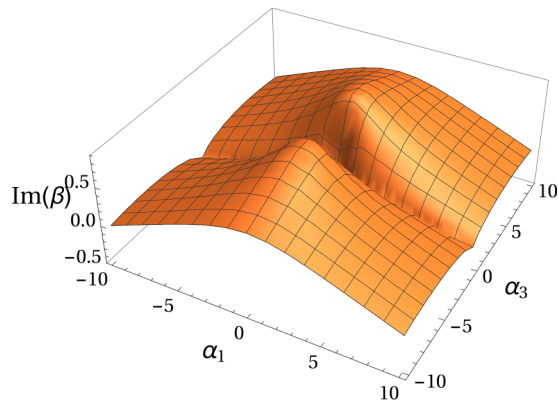


FIG. 9. Variation of  $\text{Im}(\beta)$  in three dimensions as a function of  $\alpha_1$  and  $\alpha_3$  for  $\text{Re} = 10^3$  and  $m/u_0 = 10$  for the Keplerian flow.  $\text{Im}(\beta)_{\text{max}} = 0.896$ .

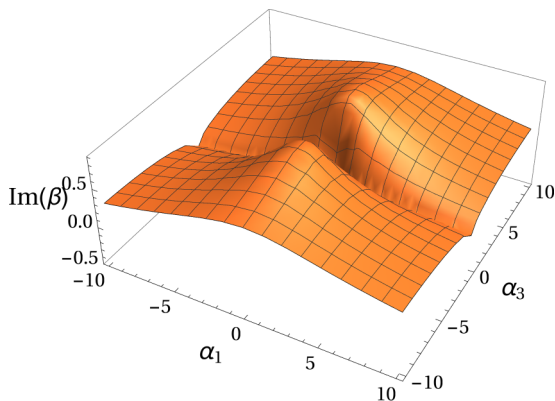


FIG. 10. Variation of  $\text{Im}(\beta)$  in three dimensions as a function of  $\alpha_1$  and  $\alpha_3$  for  $\text{Re} = 10^4$  and  $m/u_0 = 10$  for the Keplerian flow.  $\text{Im}(\beta)_{\max} = 0.91$ .

saturation of  $\text{Im}(\beta)$  depends on  $m/u_0$ . Figure 6 shows the variation of  $\text{Im}(\beta)$  as a function of  $\alpha_1$  and  $\alpha_3$  for  $\text{Re} = 10^4$  and  $m/u_0 = 10^2$  in the case of Keplerian flow. In this case,  $\text{Im}(\beta)_{\max}$  is 2.12. Increment of  $m/u_0$ , therefore, increases the saturation in  $\text{Im}(\beta)_{\max}$ . This situation is well depicted in Fig. 11, which shows the variation of  $\text{Im}(\beta)_{\max}$  as a function of  $\text{Re}$  for  $m/u_0 = 10$  and  $m/u_0 = 100$  for the Keplerian flow. In addition, the same figure shows the saturation of  $\text{Im}(\beta)_{\max}$  for a fixed  $m/u_0$ . If we consider  $\alpha_1 = 0$  in Eq. (11), we obtain the dispersion relations as shown by Nath and Mukhopadhyay [50] in their Figure 2.

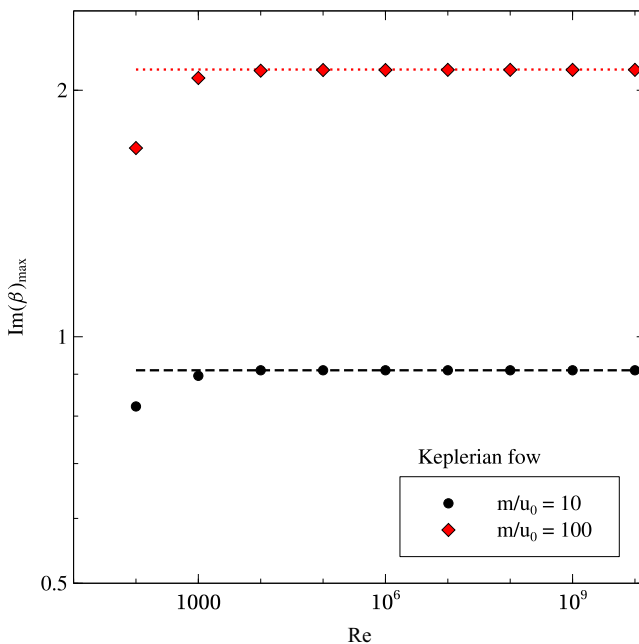


FIG. 11. Variation of  $\text{Im}(\beta)_{\max}$  as a function of  $\text{Re}$  for  $m/u_0 = 10$  and  $m/u_0 = 100$  for the Keplerian flow. The dashed and dotted lines represent  $\text{Im}(\beta)_{\max} = 0.91$  and 2.12, respectively.

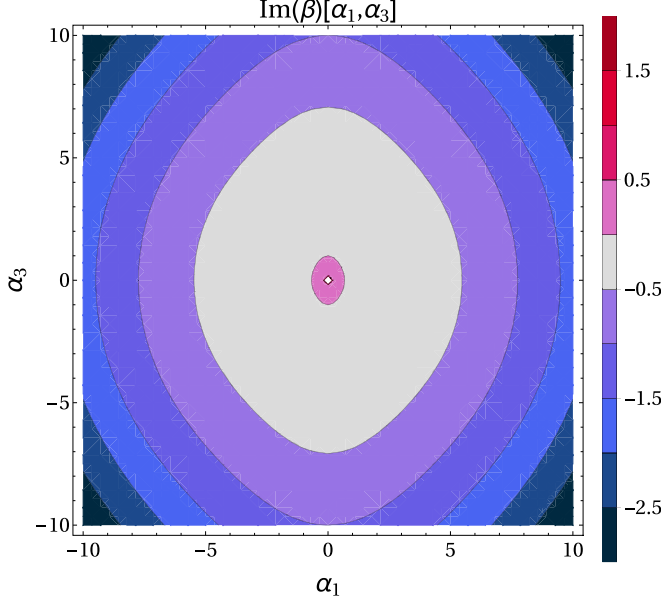


FIG. 12. Variation of  $\text{Im}(\beta)$  as a function of  $\alpha_1$  and  $\alpha_3$  for  $\text{Re} = 10^2$  and  $m/u_0 = -10^{-2}$  for plane Couette flow. At  $\alpha_1 = \alpha_3 = 0$ ,  $\text{Im}(\beta) \rightarrow \infty$ . It is indicated by a white point at the center of the plot.

### B. Plane Couette flow

For plane Couette flow, Eq. (11) becomes

$$\beta = -\frac{0.5i}{3\alpha_1^2 + \alpha_3^2} \left[ \frac{m}{u_0} + \frac{14\alpha_1^4}{\text{Re}} + \frac{12\alpha_3^2\alpha_1^2}{\text{Re}} + \frac{2\alpha_3^4}{\text{Re}} - \frac{1}{\text{Re}} \left( \frac{m^2\text{Re}^2}{u_0^2} - \frac{8\alpha_1^4 m\text{Re}}{u_0} + 16\alpha_1^8 \right)^{\frac{1}{2}} \right]. \quad (12)$$

It is quite obvious that  $\beta$  is an imaginary quantity for plane Couette flow. To have instability, therefore, the quantity within the square bracket must be negative, and this leads to the condition

$$\frac{m}{u_0} < -\frac{45}{\text{Re}(9\alpha_1^4 + 6\alpha_1^2\alpha_3^2 + \alpha_3^4)} (\alpha_1^8 + 1.867\alpha_1^6\alpha_3^2 + 1.111\alpha_1^4\alpha_3^4 + 0.267\alpha_1^2\alpha_3^6 + 0.022\alpha_3^8). \quad (13)$$

$m/u_0$ , therefore, has to be negative to have instability in plane Couette flow. If we make  $\alpha_1 = 0$ , the condition in Eq. (13) becomes

$$\frac{m}{u_0} < -\frac{\alpha_3^4}{\text{Re}}, \quad (14)$$

which was obtained by Nath and Mukhopadhyay (2016) [50] for vertical perturbation.

From Eq. (12) it is obvious that  $\text{Im}(\beta)$  blows up at  $\alpha_1 = \alpha_3 = 0$ . The color bars in the contour plots corresponding to plane Couette flow, therefore, have different meaning than indicating the value of  $\text{Im}(\beta)$ . They, rather, indicate the range of  $\alpha_1$  and  $\alpha_3$  within which  $\text{Im}(\beta)$  has positive value, i.e., flow is unstable.

We use the same color codes for the contour plots in Figs. 12, 13, 16, and 17, as used in Sec. III A. However, we use gray to indicate the transition from the positive to negative of  $\text{Im}(\beta)$ . As  $\alpha_1, \alpha_3 \rightarrow 0$ ,  $\text{Im}(\beta) \rightarrow \infty$ . The region where  $\alpha_1, \alpha_3 \rightarrow 0$ , therefore, cannot be captured in the contour plots. This region, therefore, is covered with white by default. However, to avoid any

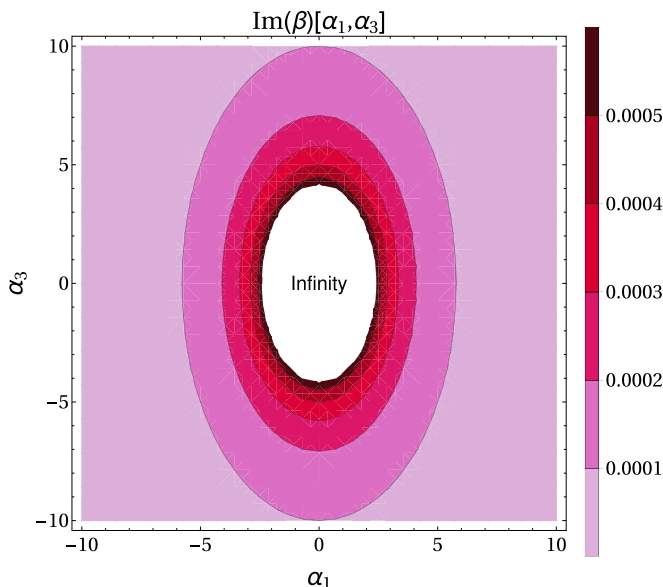


FIG. 13. Variation of  $\text{Im}(\beta)$  as a function of  $\alpha_1$  and  $\alpha_3$  for  $\text{Re} = 10^{10}$  and  $m/u_0 = -10^{-2}$  for plane Couette flow.

confusion, we mention “Infinity” inside this region wherever possible, otherwise we mention it in the corresponding captions.

Figures 12 and 13 show the variation of  $\text{Im}(\beta)$  as a function of  $\alpha_1$  and  $\alpha_3$  for  $m/u_0 = -10^{-2}$ ,  $\text{Re} = 10^2$  and  $10^{10}$ , respectively, for plane Couette flow. There is no negative  $\text{Im}(\beta)$  in Fig. 13 within the ranges of  $\alpha_1$  and  $\alpha_3$ . On the contrary, there are negative values of  $\text{Im}(\beta)$  in Fig. 12 within the same range of  $\alpha_1$  and  $\alpha_3$ . For the same  $m/u_0$  (which is also very small here), therefore, the increment in  $\text{Re}$  increases the range of  $\alpha_1$  and  $\alpha_3$ , which gives rise to positive  $\text{Im}(\beta)$  and hence increases the chance of making the system unstable. Figures 14 and 15 make this point even clearer. These two figures represent the variation of  $\text{Im}(\beta) (\geq 0)$  in three dimensions as a function of  $\alpha_1$  and  $\alpha_3$  for  $\text{Re} = 10^2$  and  $10^{10}$ , respectively, for  $m/u_0 = -10^{-2}$  for plane Couette flow.

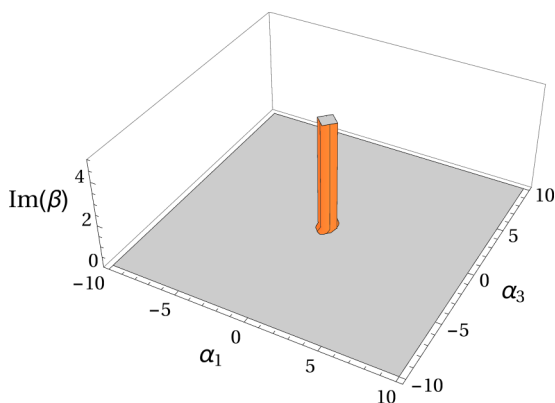


FIG. 14. Variation of  $\text{Im}(\beta)$  in three dimensions as a function of  $\alpha_1$  and  $\alpha_3$  for  $\text{Re} = 10^2$  and  $m/u_0 = -10^{-2}$  for plane Couette flow.

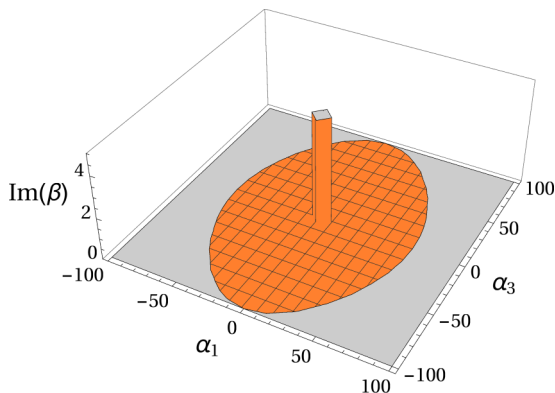


FIG. 15. Variation of  $\text{Im}(\beta)$  in three dimensions as a function of  $\alpha_1$  and  $\alpha_3$  for  $\text{Re} = 10^{10}$  and  $m/u_0 = -10^{-2}$  for plane Couette flow.

It is also expected that if we increase the magnitude of  $m/u_0$ , the system becomes more unstable as in the case of Keplerian flow. This phenomenon also happens here but in a different way. Figures 16 and 17 show the variation of  $\text{Im}(\beta)$  as a function of  $\alpha_1$  and  $\alpha_3$  for  $\text{Re} = 10^2$  and  $10^{10}$ , respectively, and for  $m/u_0 = -10$  for plane Couette flow. However, if we compare carefully Fig. 12 (or Fig. 13) with Fig. 16 (or Fig. 17), we see that Fig. 16 (or Fig. 17) has a larger range of  $\alpha_1$  and  $\alpha_3$  to give rise to positive  $\text{Im}(\beta)$ .

#### IV. ARGAND DIAGRAM

The time variation of the perturbations is given by

$$u, \zeta \sim e^{-i\text{Re}(\beta)t} e^{\text{Im}(\beta)t}. \quad (15)$$

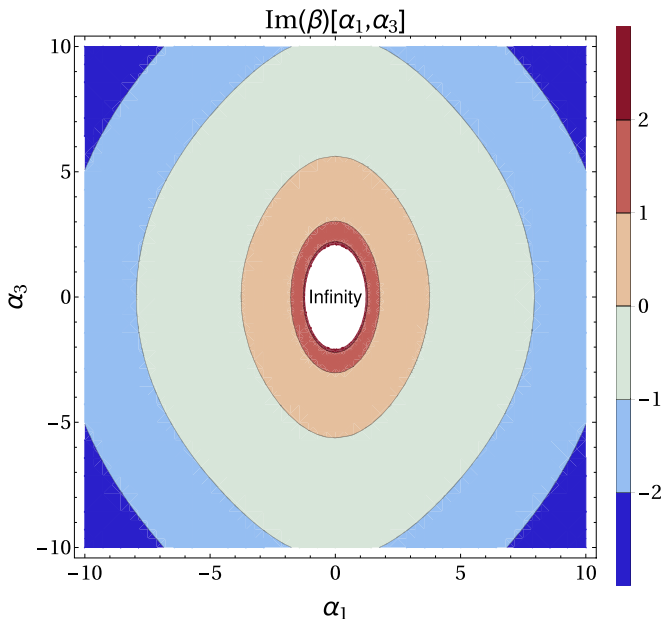


FIG. 16. Variation of  $\text{Im}(\beta)$  as a function of  $\alpha_1$  and  $\alpha_3$  for  $\text{Re} = 10^2$  and  $m/u_0 = -10$  for plane Couette flow.

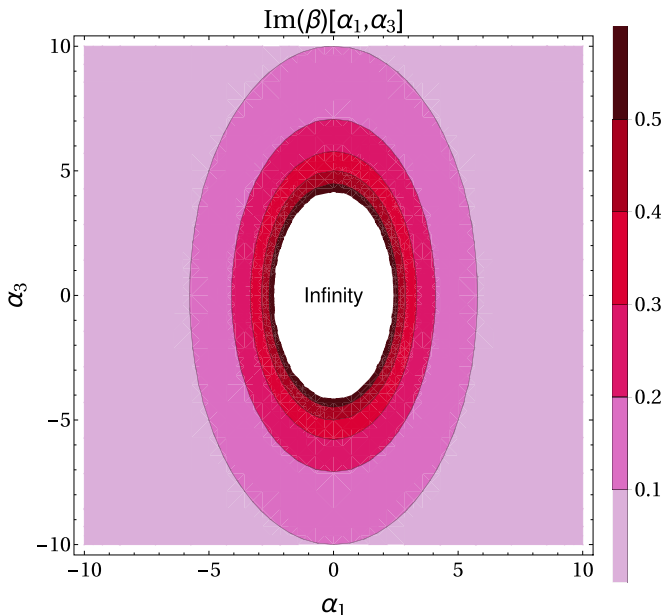


FIG. 17. Variation of  $\text{Im}(\beta)$  as a function of  $\alpha_1$  and  $\alpha_3$  for  $\text{Re} = 10^{10}$  and  $m/u_0 = -10$  for plane Couette flow.

In Sec. III we show that  $\text{Im}(\beta)$  has a positive value within a certain range of  $\alpha_1$  and  $\alpha_3$ . For those values of  $\alpha_1$  and  $\alpha_3$ , therefore,  $e^{[\text{Im}(\beta)]t}$  increases exponentially with time. On the other hand,  $e^{-i[\text{Re}(\beta)]t}$  is oscillatory in time. The real part of the temporal variation of the perturbation is

$$\text{Re}(u), \text{Re}(\zeta) \sim \cos[\text{Re}(\beta)t]e^{\text{Im}(\beta)t}. \quad (16)$$

Here we observe the variation of  $\text{Im}(\beta)$  as a function of  $\text{Re}(\beta)$ . Figure 18 shows Argand diagrams for  $\text{Re} = 10, 10^2, 10^3$  for fixed  $\alpha_1 (=1)$  and  $m/u_0 = 10$  by varying  $\alpha_3$  in case of the Keplerian flow. We observe that  $\text{Im}(\beta)_{\text{max}}$ , i.e., the maximum growth rate, increases as we increase  $\text{Re}$  for a fixed  $m/u_0$ . Figure 19 shows the Argand diagrams for  $\text{Re} = 10^4, m/u_0 = 10$  and for  $\alpha_1 = 1.0, 5.0$  and  $10.0$  for the Keplerian flow, where for each  $\alpha_1$ , we vary  $\alpha_3$  from  $-2000$  to  $2000$ . From Fig. 19 it is clear that as we decrease  $\alpha_1$ ,  $\text{Im}(\beta)_{\text{max}}$  increases. For smaller  $\alpha_1$ , therefore, the system becomes unstable at smaller time and plausibly becomes turbulent for those  $\alpha_1$  first.

The phenomenon of increment in the maximum growth rate with decreasing  $\alpha_1$  is described through the energy of perturbations in Fig. 20. Here  $[\text{Re}(u)]^2$  represents the temporal evolution of energy corresponding to the  $x$  component of the perturbed velocity field for  $\text{Im}(\beta)_{\text{max}}$  and  $\text{Re}(\beta)_{\text{max}}$  corresponding to three different  $\alpha_1$ ,  $\text{Re} = 10^4$  for  $m/u_0 = 10$  in the case of the Keplerian flow. In Fig. 20 the maximum value along the vertical axis is  $10^4$ . We consider this value to be the limit of linearity following Ref. [45]. We notice that the higher  $\text{Im}(\beta)_{\text{max}}$  has higher  $\text{Re}(\beta)_{\text{max}}$ , i.e., the higher growth rates have the higher frequency.

It is always interesting to check what happens to the  $\text{Im}(\beta)_{\text{max}}$  if  $m/u_0$  increases for the same  $\text{Re}$ . Figure 21 shows the variation of  $\text{Im}(\beta)_{\text{max}}$  as a function of  $m/u_0$ , for  $\alpha_1 = 1, 5, 10$  for  $\text{Re} = 10^4$  for the Keplerian flow. Here we notice that  $\text{Im}(\beta)_{\text{max}}$  increases as we increase  $m/u_0$ . However, at larger  $m/u_0$ , the  $\text{Im}(\beta)_{\text{max}}$  becomes almost independent on  $\alpha_1$ . At higher  $m/u_0$ , the extra force and  $\text{Re}$  almost completely take control of the system of a fixed  $q$ . This phenomenon can be explained

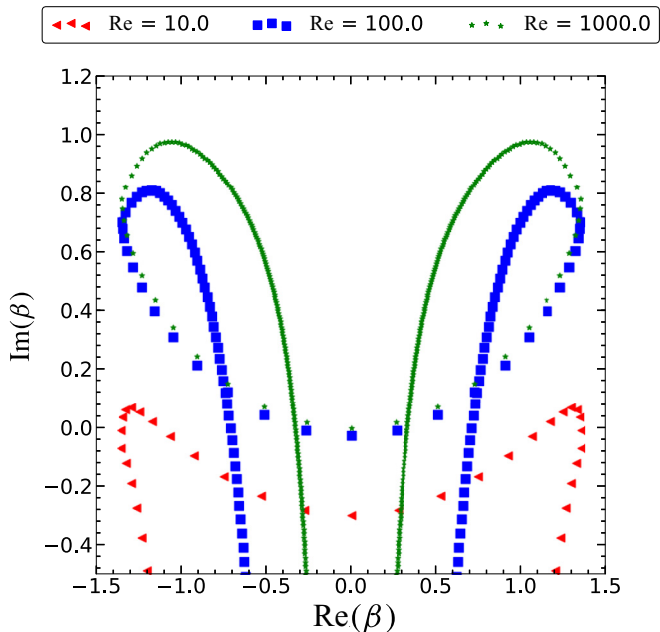


FIG. 18. Argand diagram for  $\text{Re} = 10, 100$  and  $1000$  for  $m/u_0 = 10$  and  $\alpha_1 = 1.0$  for the Keplerian flow. For each  $\text{Re}$ ,  $\alpha_3$  is varied from  $-2000$  to  $2000$ .

from (11). At large  $m/u_0$ , (11) becomes

$$\beta \sim -\frac{0.5i}{3\alpha_1^2 q + \alpha_3^2 q} \left[ \frac{mq}{u_0} - \frac{1}{\text{Re}} \left( \frac{24i\alpha_3\alpha_1^2 mq \text{Re}^2}{u_0} + \frac{8i\alpha_3^3 mq \text{Re}^2}{u_0} + \frac{m^2 q^2 \text{Re}^2}{u_0^2} - \frac{8\alpha_1^4 mq^2 \text{Re}}{u_0} \right)^{\frac{1}{2}} \right]. \quad (17)$$

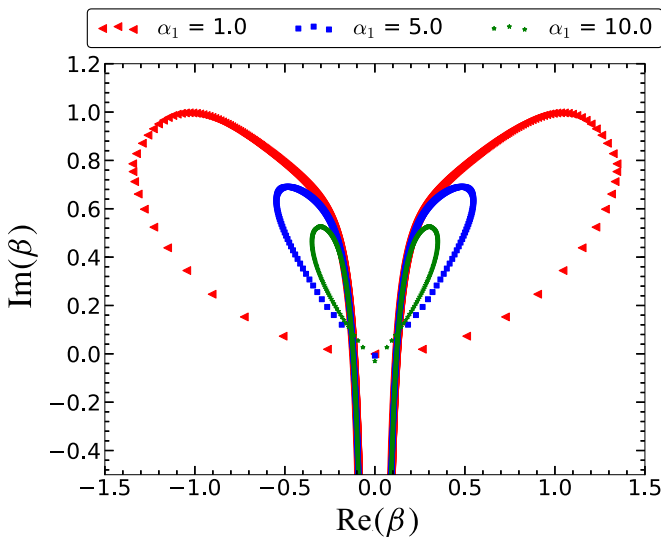


FIG. 19. Argand diagram for  $\text{Re} = 10^4$ ,  $m/u_0 = 10$  and for  $\alpha_1 = 1.0, 5.0,$  and  $10.0$  for the Keplerian flow.

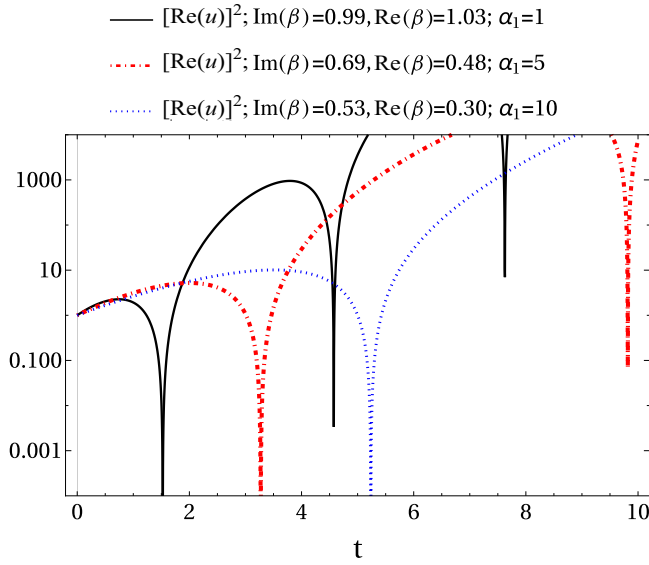


FIG. 20. Variation of  $[\text{Re}(u)]^2$  as a function of time, for  $\text{Re}(\beta)_{\max}$  and  $\text{Im}(\beta)_{\max}$  from Fig. 19 corresponding to  $\alpha_1 = 1.0, 5.0,$  and  $10.0$ .

We obtain Eq. (17) from Eq. (11) by retaining the terms that involve with  $m/u_0$  as the magnitude of other terms become negligible compared to those involving with  $m/u_0$ . From Eq. (17) it is evident that as  $m/u_0$  increases, the effect of  $\alpha_1$  on  $\beta$  and, hence,  $\text{Im}(\beta)$  decreases.

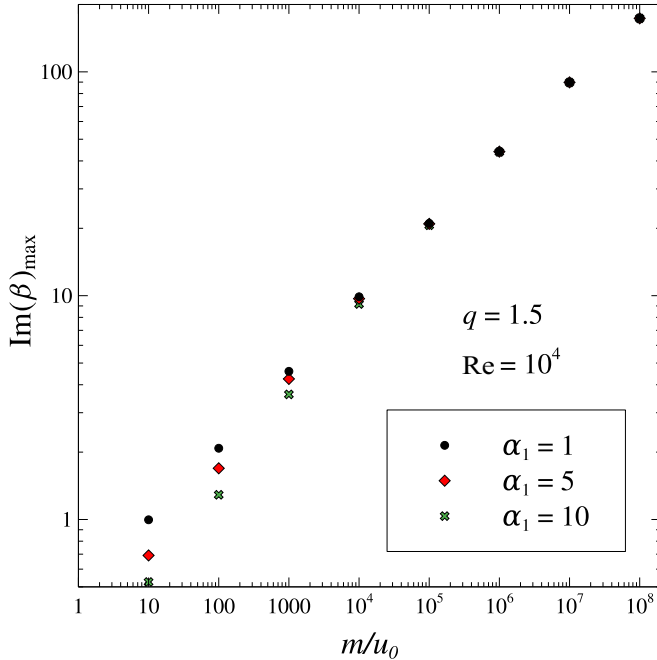


FIG. 21. Variation of  $\text{Im}(\beta)_{\max}$  as a function of  $m/u_0$ , for  $\alpha_1 = 1, 5, 10$  and  $\text{Re} = 10^4$  for the Keplerian flow.

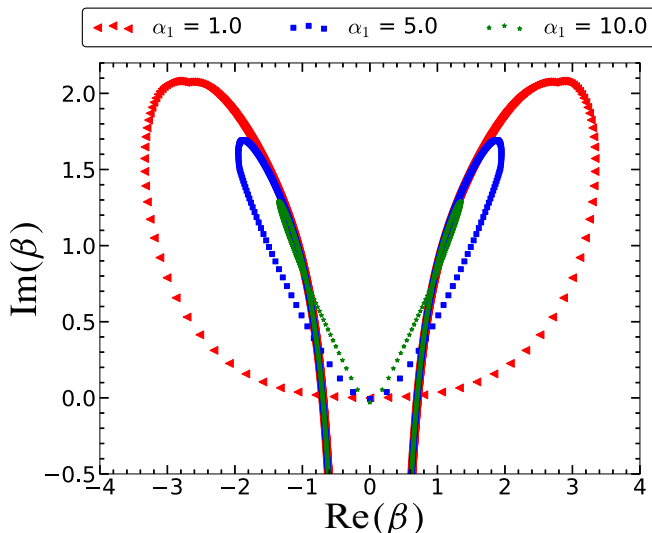


FIG. 22. Argand diagram for  $\text{Re} = 10^4$ ,  $m/u_0 = 10^2$  and for  $\alpha_1 = 1.0, 5.0$ , and  $10.0$  for the Keplerian flow.

To make the study complete, we should have enough comparison among Argand diagrams like Fig. 19 but with different  $m/u_0$  and  $\text{Re}$ . Figure 22 represents the Argand diagrams for  $\text{Re} = 10^4$  and  $m/u_0 = 10^2$  for three values of  $\alpha_1$  mentioned in the figure where  $\alpha_3$  is varied from  $-2000$  to  $2000$  for each value of  $\alpha_1$ . Here we see that,  $\text{Im}(\beta)_{\text{max}}$  and  $\text{Re}(\beta)_{\text{max}}$  for three different  $\alpha_1$  are greater than those for  $m/u_0 = 10$ . We, therefore, confirm that as  $m/u_0$  increases the values of  $\text{Im}(\beta)_{\text{max}}$  and  $\text{Re}(\beta)_{\text{max}}$  also increase. Figures 23 and 24 show the Argand diagrams for  $\text{Re} = 10^{10}$  but for  $m/u_0 = 10$  and  $10^2$ , respectively, for three different  $\alpha_1$  as shown in the corresponding figures, and for each  $\alpha_1$ , we vary  $\alpha_3$  from  $-100\,000$  to  $100\,000$ . If we compare between Figs. 19 and 23 (and between Figs. 22 and 24), we notice that  $\text{Im}(\beta)_{\text{max}}$  and  $\text{Re}(\beta)_{\text{max}}$  do not change as we increase  $\text{Re}$  for a fixed  $m/u_0$  ( $= 10$ ), but the range of  $\alpha_1$ , that gives rise to positive  $\text{Im}(\beta)$ , does increase, as the positive area under the curve increases with increasing  $\text{Re}$ .

## V. COMPARISON OF VARIOUS TIMESCALES

In Sec. III we obtain the dispersion relation for the linear perturbation in the presence of Coriolis force and extra force for the Keplerian flow as well as plane Couette flow. It shows that there is a range of wave vectors in which  $\text{Im}(\beta)$  is positive. On the other hand, we also see the presence of temporal oscillation in the linear perturbation due to the presence of  $\text{Re}(\beta)$  in Sec. IV. It, therefore, is important to compare the time period of the temporal growth of the perturbation with the infall timescale. To calculate the infall timescale of the fluid parcel, we need the radial component of velocity of the flow in the Keplerian disk, and it is given by (see e.g., Ref. [7])

$$v_r(R) = 2.7 \times 10^4 \times \alpha_s^{4/5} \left( \frac{\dot{M}}{10^{16}} \right)^{3/10} \left( \frac{M}{M_\odot} \right)^{-1/4} \left( \frac{R}{10^{10}} \right)^{-1/4} \left[ 1 - \left( \frac{R_*}{R} \right)^{1/2} \right]^{-7/10} \text{ cm s}^{-1}, \quad (18)$$

where  $\alpha_s$  is the Shakura-Sunyaev viscosity parameter,  $\dot{M}$  is the mass accretion rate,  $M$  is the mass of the accretor,  $R$  is the radius where the analysis is done,  $R_*$  is the radius of the accretor and for a nonrotating black hole it will be the Schwarzschild radius ( $R_s = 2GM/c^2$ , where  $G$  is gravitational constant,  $c$  is the speed of light in free space), and  $M_\odot$  is the solar mass. The time it takes for a fluid parcel to reach  $3R_s$  from  $100R_s$  for a  $10M_\odot$  accretor is  $\sim 8 \times 10^3$  s, if  $\alpha_s = 0.1$ . The time period of the perturbations will be  $[2\pi/\text{Re}(\beta)_{\text{max}}] \sqrt{R^3/GMq^2}$  s. From Fig. 19 we obtain  $\text{Re}(\beta)_{\text{max}}$  to be 1.03,

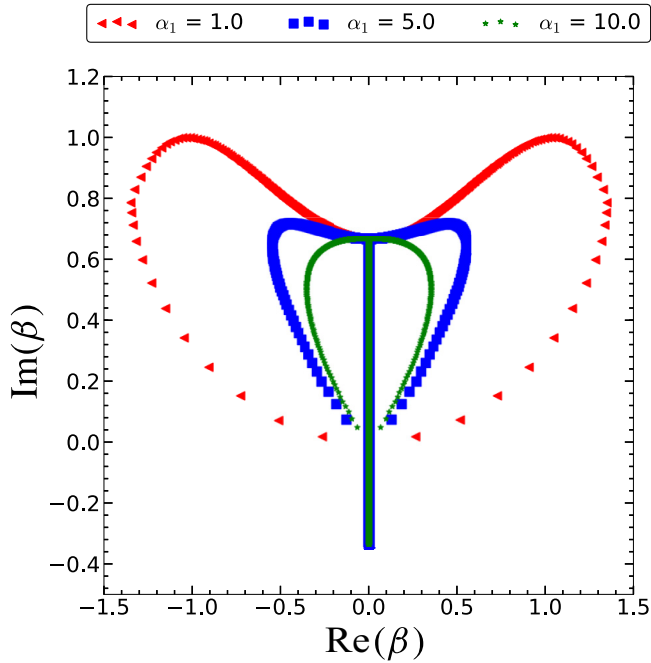


FIG. 23. Argand diagram for  $\text{Re} = 10^{10}$ ,  $m/u_0 = 10$  and for  $\alpha_1 = 1.0, 5.0$ , and  $10.0$  for the Keplerian flow.

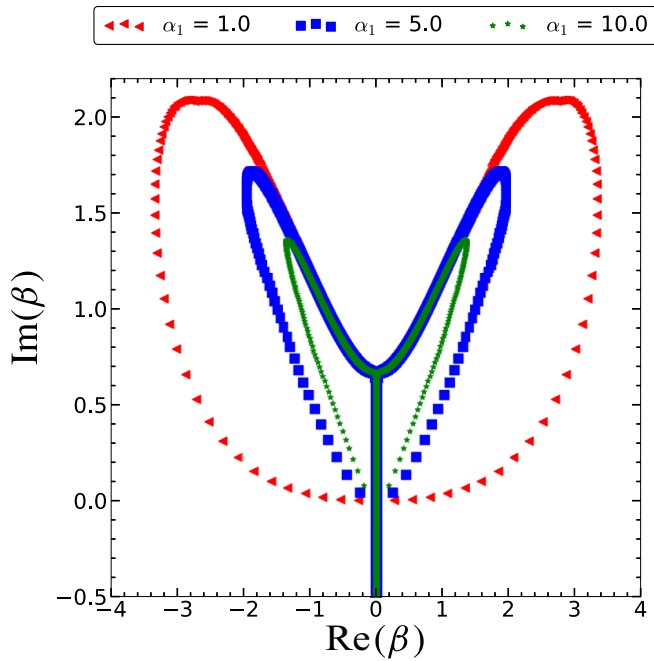


FIG. 24. Argand diagram for  $\text{Re} = 10^{10}$ ,  $m/u_0 = 10^2$  and for  $\alpha_1 = 1.0, 5.0$ , and  $10.0$  for the Keplerian flow.

0.48, and 0.3 for  $\alpha_1$  to be 1, 5, and 10, respectively. The time period corresponding to these cases will be 0.57, 1.22, and 1.95 s, respectively. These timescales are very tiny in comparison with the infall timescale of the matter to fall from  $100R_s$ ; i.e., the fluid parcel gets enough time to be unstable before it ultimately falls into the black hole. Our theory, therefore, passes the first check.

Now the crucial and more important point is how much time the fluid parcel takes to cross the shearing box itself along the radial direction. We consider the size of the shearing box to be  $0.05R_s$  (see Ref. [18]), and it is situated at  $100R_s$ . With these configurations, the fluid parcel takes around 5.34 s to cross the box. This timescale is also greater than the time period of the temporal oscillation of the perturbation.

Apart from the timescale corresponding to temporal oscillation of the perturbation, there is another timescale involved in the system, and it is at which time the system enters into the nonlinear regime. From Fig. 20, it is clear that  $[\text{Re}(u)]^2$  for  $\alpha_1 = 10$  enters into the nonlinear regime for the first time at  $t \sim 9$ . To convert it into the unit of second, we have to multiply it with a factor  $\sqrt{R^3/GMq^2}$ , which is around 0.09 s for the considered system. It, therefore, takes around 0.8 s for the fluid parcel to enter into the nonlinear regime if we consider  $\alpha_1 = 10$ ,  $\text{Re} = 10^4$ ,  $m/u_0 = 10$ .

It is very important to have the wavelength of the perturbation inside the box. It, therefore, is necessary to have the maximum wavelength of the perturbation to be equal to the size of the box. The wavelength of the perturbation along the  $x$  direction is  $2\pi/\alpha_1$  in dimensionless units. To make it dimensional, we have to multiply the size of the box ( $0.05R_s$ ) with it. Those  $\alpha_1$  which are greater than  $2\pi$ , therefore, describe the best dynamics of the fluid parcel inside the box. This is the reason behind showing the temporal evolution of  $[\text{Re}(u)]^2$  with corresponding  $\text{Im}(\beta)_{\text{max}}$  and  $\text{Re}(\beta)_{\text{max}}$  for fixed  $\text{Re}$  and  $\alpha_1 = 10 (>2\pi)$  for  $m/u_0 = 10$  and  $10^2$ .

## VI. CONCLUSION

Instability and hence turbulence become inevitable for the fluid parcel inside the shearing box at the small region of the accretion disk. This instability is also controlled by  $\text{Re}$  and the strength of the extra force which is white noise with nonzero mean ( $m$ ). The presence of noise is very natural. It may arise from small thermal fluctuation present in the systems (see, e.g., Ref. [50]). The presence of the noise in the systems can be due to the disturbances of arbitrary origins [51]. However, in the astrophysical context, particularly in accretion disks, the examples of the origin of such forces could be the interaction between the dust grains and the fluid parcel in protoplanetary disks (e.g., Ref. [52]); back reactions of outflow/jet to accretion disks; and external forcing of the disk, i.e., tidal forcing, shock wave debris, outbursts, or internal forcing by nonlinear terms [53,54]. These forces are also expected to be stochastic in nature.

Once the instability and therefore turbulence kick in inside the shearing box, we consider the shearing box repeatedly throughout the radial extension of the accretion disk, and hence the transport of angular momentum can be interpreted in the Keplerian accretion disk. However, for plane Couette flow, there is no requirement of infall. Hence, in the presence of noise, it is always expected to lead to instability.

## ACKNOWLEDGMENTS

S.G. acknowledges DST India for the INSPIRE fellowship. The authors are thankful to the referees for their comments and suggestions, which helped present the work better. This work is partly supported by a fund of the Department of Science and Technology (DST-SERB) with research Grant No. DSTO/PPH/BMP/1946 (EMR/2017/001226).

**APPENDIX: DISPERSION RELATIONS FROM ORR-SOMMERFELD AND SQUIRE EQUATIONS IN THE FOURIER SPACE**

The solutions of Eqs. (1) and (2) in the Fourier space will be

$$\begin{aligned}\tilde{\psi}_{\mathbf{k},\omega} &= \left(\frac{1}{2\pi}\right)^4 \int_{-\infty}^{\infty} \psi(x) e^{i(\alpha\mathbf{r}-\beta t)} e^{-i(\mathbf{k}\cdot\mathbf{r}-\omega t)} d^3x dt \\ &= \frac{1}{2\pi} \delta(\alpha_2 - k_y) \delta(\alpha_3 - k_z) \delta(\beta - \omega) \int_{-\infty}^{\infty} \psi(x) e^{i(\alpha_1 - k_x)x} dx,\end{aligned}$$

where  $\psi$  will be any of  $u$  and  $\zeta$ .

We now integrate Eqs. (6) and (7) with respect to  $\mathbf{k}$  and  $\omega$ . Each term of Eq. (6) after the integration, assuming the WKB approximation, i.e., neglecting second and higher derivatives of  $u$  and  $\zeta$ , is obtained as follows:

(1)

$$\begin{aligned}\int_{-\infty}^{\infty} k_y k^2 \frac{\partial \tilde{u}_{\mathbf{k},\omega}}{\partial k_x} d^3k d\omega &= \int_{-\infty}^{\infty} k_y (k_x^2 + k_y^2 + k_z^2) \frac{\partial \tilde{u}_{\mathbf{k},\omega}}{\partial k_x} d^3k d\omega \\ &= \frac{1}{2\pi} \int_{-\infty}^{\infty} k_y (k_x^2 + k_y^2 + k_z^2) \delta(\alpha_2 - k_y) \delta(\alpha_3 - k_z) \\ &\quad \times \left[ \frac{\partial}{\partial k_x} \int_{-\infty}^{\infty} dx' u(x') e^{i(\alpha_1 - k_x)x'} \right] dk_x dk_y dk_z \\ &= -2\alpha_1 \alpha_2 u(0) + 2i\alpha_2 u'(0),\end{aligned}$$

(2)

$$\int_{-\infty}^{\infty} i\omega k^2 \tilde{u}_{\mathbf{k},\omega} d^3k d\omega = i\beta[\alpha^2 u(0) - 2i\alpha_1 u'(0)],$$

(3)

$$\int_{-\infty}^{\infty} 2k_x k_y \tilde{u}_{\mathbf{k},\omega} d^3k d\omega = -2i\alpha_2 [u'(0) + i\alpha_1 u(0)],$$

(4)

$$\int_{-\infty}^{\infty} \frac{k^4}{\text{Re}} \tilde{u}_{\mathbf{k},\omega} d^3k d\omega = \frac{\alpha^4}{\text{Re}} u(0) - \frac{4}{\text{Re}} i\alpha_1 \alpha^2 u'(0),$$

(5)

$$\int_{-\infty}^{\infty} \frac{2ik_z}{q} \tilde{\zeta}_{\mathbf{k},\omega} d^3k d\omega = \frac{2i\alpha_3}{q} \zeta_0,$$

(6)

$$\int_{-\infty}^{\infty} m_1 \delta(\mathbf{k}) \delta(\omega) d^3k d\omega = m_1.$$

We collect all these terms and obtain the first part of Eq. (9). Following the same method, we also obtain the second part of Eq. (9) from Eq. (7).

- 
- [1] S. A. Orszag, Accurate solution of the Orr-Sommerfeld stability equation, *J. Fluid Mech.* **50**, 689 (1971).  
 [2] V. A. Romanov, Stability of plane-parallel Couette flow, *Funct. Anal. Appl.* **7**, 137 (1973).

- [3] F. Alavyoon, D. S. Henningson, and P. H. Alfredsson, Turbulent spots in plane Poiseuille flow-flow visualization, *Phys. Fluids* **29**, 1328 (1986).
- [4] S. Grossmann, The onset of shear flow turbulence, *Rev. Mod. Phys.* **72**, 603 (2000).
- [5] O. Dauchot and F. Daviaud, Finite-amplitude perturbation in plane Couette flow, *Europhys. Lett.* **28**, 225 (1994).
- [6] Y. Duguet, P. Schlatter, and D. S. Henningson, Formation of turbulent patterns near the onset of transition in plane Couette flow, *J. Fluid Mech.* **650**, 119 (2010).
- [7] J. Frank, A. King, and D. J. Raine, *Accretion Power in Astrophysics*, 3rd ed. (Cambridge University Press, Cambridge, UK, 2002), p. 398.
- [8] N. I. Shakura and R. A. Sunyaev, Black holes in binary systems. Observational appearance, *Astron. Astrophys.* **500**, 33 (1973).
- [9] D. Lynden-Bell and J. E. Pringle, The evolution of viscous discs and the origin of the nebular variables, *Mon. Not. R. Astron. Soc.* **168**, 603 (1974).
- [10] S. A. Balbus and J. F. Hawley, A powerful local shear instability in weakly magnetized disks. I—Linear analysis, *Astrophys. J.* **376**, 214 (1991).
- [11] E. P. Velikhov, Stability of an ideally conducting liquid flowing between rotating cylinders in a magnetic field, *Zh. Eksp. Teor. Fiz.* **36**, 5 (1959).
- [12] S. Chandrasekhar, The stability of non-dissipative Couette flow in hydromagnetics, *Proc. Natl. Acad. Sci. USA* **46**, 253 (1960).
- [13] X.-N. Bai, Wind-driven accretion in protoplanetary disks. II. Radial dependence and global picture, *Astrophys. J.* **772**, 96 (2013).
- [14] X.-N. Bai, Global simulations of the inner regions of protoplanetary disks with comprehensive disk microphysics, *Astrophys. J.* **845**, 75 (2017).
- [15] C. F. Gammie and K. Menou, On the origin of episodic accretion in dwarf novae, *Astrophys. J.* **492**, L75 (1998).
- [16] K. Menou, Viscosity mechanisms in accretion disks, *Science* **288**, 2022 (2000).
- [17] K. Menou and E. Quataert, Ionization, magnetorotational, and gravitational instabilities in thin accretion disks around supermassive black holes, *Astrophys. J.* **552**, 204 (2001).
- [18] S. K. Nath and B. Mukhopadhyay, Origin of nonlinearity and plausible turbulence by hydromagnetic transient growth in accretion disks: Faster growth rate than magnetorotational instability, *Phys. Rev. E* **92**, 023005 (2015).
- [19] B. Mukhopadhyay, Can the viscosity in astrophysical black hole accretion disks be close to its string theory bound?, *Phys. Lett. B* **721**, 151 (2013).
- [20] T. S. Bhatia and B. Mukhopadhyay, Exploring non-normality in magnetohydrodynamic rotating shear flows: Application to astrophysical accretion disks, *Phys. Rev. Fluids* **1**, 063101 (2016).
- [21] M. E. Pessah and D. Psaltis, The stability of magnetized rotating plasmas with superthermal fields, *Astrophys. J.* **628**, 879 (2005).
- [22] U. Das, M. C. Begelman, and G. Lesur, Instability in strongly magnetized accretion discs: A global perspective, *Mon. Not. Roy. Astron. Soc.* **473**, 2791 (2018).
- [23] B. Dubrulle, O. Dauchot, F. Daviaud, P. Y. Longaretti, D. Richard, and J. P. Zahn, Stability and turbulent transport in Taylor-Couette flow from analysis of experimental data, *Phys. Fluids* **17**, 095103 (2005).
- [24] B. Dubrulle, L. Marié, Ch. Normand, D. Richard, F. Hersant, and J.-P. Zahn, A hydrodynamic shear instability in stratified disks, *Astron. Astrophys.* **429**, 1 (2005).
- [25] O. Dauchot and F. Daviaud, Finite amplitude perturbation and spots growth mechanism in plane Couette flow, *Phys. Fluids* **7**, 335 (1995).
- [26] G. Rüdiger and Y. Zhang, MHD instability in differentially-rotating cylindrical flows, *Astron. Astrophys.* **378**, 302 (2001).
- [27] H. H. Klahr and P. Bodenheimer, Turbulence in accretion disks: Vorticity generation and angular momentum transport via the global baroclinic instability, *Astrophys. J.* **582**, 869 (2003).
- [28] D. Richard and J.-P. Zahn, Turbulence in differentially rotating flows what can be learned from the Couette-Taylor experiment, *Astron. Astrophys.* **347**, 734 (1999).

- [29] W.-T. Kim and E. C. Ostriker, Magnetohydrodynamic instabilities in shearing, rotating, stratified winds and disks, *Astrophys. J.* **540**, 372 (2000).
- [30] S. M. Mahajan and V. Krishan, Existence of the magnetorotational instability, *Astrophys. J.* **682**, 602 (2008).
- [31] P. A. Yecko, Accretion disk instability revisited—Transient dynamics of rotating shear flow, *Astron. Astrophys.* **425**, 385 (2004).
- [32] G. Lesur and J. C. B. Papaloizou, The subcritical baroclinic instability in local accretion disk models, *Astron. Astrophys.* **513**, A60 (2010).
- [33] B. Mukhopadhyay, R. Mathew, and S. Raha, Growing pseudo-eigenmodes and positive logarithmic norms in rotating shear flows, *New J. Phys.* **13**, 023029 (2011).
- [34] B. Mukhopadhyay and A. K. Chattopadhyay, Stochastically driven instability in rotating shear flows, *J. Phys. A: Math. Gen.* **46**, 035501 (2013).
- [35] S. A. Balbus, J. F. Hawley, and J. M. Stone, Nonlinear stability, hydrodynamical turbulence, and transport in disks, *Astrophys. J.* **467**, 76 (1996).
- [36] J. F. Hawley, S. A. Balbus, and W. F. Winters, Local hydrodynamic stability of accretion disks, *Astrophys. J.* **518**, 394 (1999).
- [37] G. Lesur and P.-Y. Longaretti, On the relevance of subcritical hydrodynamic turbulence to accretion disk transport, *Astron. Astrophys.* **444**, 25 (2005).
- [38] A. Pumir, Turbulence in homogeneous shear flows, *Phys. Fluids* **8**, 3112 (1996).
- [39] S. Fromang and J. Papaloizou, MHD simulations of the magnetorotational instability in a shearing box with zero net flux—I. The issue of convergence, *Astron. Astrophys.* **476**, 1113 (2007).
- [40] F. Nauman and M. E. Pessah, Sustained turbulence in differentially rotating magnetized fluids at a low magnetic Prandtl number, *Astrophys. J.* **833**, 187 (2016).
- [41] J.-M. Shi, J. M. Stone, and C. X. Huang, Saturation of the magnetorotational instability in the unstratified shearing box with zero net flux: Convergence in taller boxes, *Mon. Not. R. Astron. Soc.* **456**, 2273 (2015).
- [42] J. Walker, G. Lesur, and S. Boldyrev, On the nature of magnetic turbulence in rotating, shearing flows, *Mon. Not. R. Astron. Soc. Lett.* **457**, L39 (2016).
- [43] M. S. Paoletti, D. P. M. van Gils, B. Dubrulle, C. Sun, D. Lohse, and D. P. Lathrop, Angular momentum transport and turbulence in laboratory models of Keplerian flows, *Astron. Astrophys.* **547**, A64 (2012).
- [44] M. Avila, Stability and Angular-Momentum Transport of Fluid Flows between Corotating Cylinders, *Phys. Rev. Lett.* **108**, 124501 (2012).
- [45] B. Mukhopadhyay, N. Afshordi, and R. Narayan, Bypass to turbulence in hydrodynamic accretion disks: An eigenvalue approach, *Astrophys. J.* **629**, 383 (2005).
- [46] N. Afshordi, B. Mukhopadhyay, and R. Narayan, Bypass to turbulence in hydrodynamic accretion: Lagrangian analysis of energy growth, *Astrophys. J.* **629**, 373 (2005).
- [47] C. D. Cantwell, D. Barkley, and H. M. Blackburn, Transient growth analysis of flow through a sudden expansion in a circular pipe, *Phys. Fluids* **22**, 034101 (2010).
- [48] D. Forster, D. R. Nelson, and M. J. Stephen, Large-distance and long-time properties of a randomly stirred fluid, *Phys. Rev. A* **16**, 732 (1977).
- [49] C. DeDominicis and P. C. Martin, Energy spectra of certain randomly-stirred fluids, *Phys. Rev. A* **19**, 419 (1979).
- [50] S. K. Nath and B. Mukhopadhyay, A pure hydrodynamic instability in shear flows and its application to astrophysical accretion disks, *Astrophys. J.* **830**, 86 (2016).
- [51] B. F. Farrell and P. J. Ioannou, Stochastic forcing of the linearized Navier-Stokes equations, *Phys. Fluids A* **5**, 2600 (1993).
- [52] T. Henning and R. Stognienko, Dust opacities for protoplanetary accretion disks—Influence of dust aggregates, *Astron. Astrophys.* **311**, 291 (1996).
- [53] P. J. Ioannou and A. Kakouris, Stochastic dynamics of Keplerian accretion disks, *Astrophys. J.* **550**, 931 (2001).
- [54] D. N. Razdoburdin, Perturbations dynamics in Keplerian flow under external stochastic forcing, *Mon. Not. R. Astron. Soc.* **492**, 5366 (2020).